Broadband nano-focusing of light using kissing nanowires



2010 New J. Phys. 12 093030

(http://iopscience.iop.org/1367-2630/12/9/093030)

New Journal of Physics
The open-access journal for physics

# Broadband nano-focusing of light using kissing nanowires

**Dang Yuan Lei**[1], **Alexandre Aubry, Stefan A Maier and John B Pendry**

The Blackett Laboratory, Department of Physics, Imperial College London, London SW7 2AZ, UK
E-mail: dangyuan.lei08@imperial.ac.uk

*New Journal of Physics* **12** (2010) 093030 (20pp)
Received 10 June 2010
Published 22 September 2010
Online at http://www.njp.org/
doi:10.1088/1367-2630/12/9/093030

**Abstract.** A strategy has been proposed recently to design plasmonic nanostructures capable of efficient harvesting of light over a broadband spectrum. Applying a singular conformal transformation to a metal–insulator–metal infinite structure, the optical response of two kissing nanowires can be deduced analytically. This nanostructure is shown to exhibit a large and continuous absorption cross-section relative to its physical size over the whole visible spectrum. Considerable field enhancement and confinement at the nano-scale are also expected at the touching point. Actually, instead of transporting the energy out to infinity, like in a metal slab geometry, the surface plasmon modes here propagate towards the singularity of the structure where their velocity vanishes and energy accumulates. The field enhancement is then a balance between this energy accumulation and dissipation losses. The asymptotic case of a nanowire placed on top of a metal plate is shown to be of great interest for nanofocusing. Finally, numerical simulations are performed to investigate the effect of radiative losses when the structure dimension becomes comparable to the wavelength.

[1] Author to whom any correspondence should be addressed.

## Contents



## 1. Introduction

Metallic nanostructures have shown an unprecedented ability to concentrate light into subwavelength volumes when surface plasmon modes are excited in these structures at their resonant wavelengths [1, 2]. In particular, plasmon nanofocusing can be obtained at the tip of a tapered metallic guiding nanostructure where a dramatic field enhancement may arise [3]. On the one hand, this extreme light concentration and manipulation at the nanoscale have found applications in single molecule detection [4, 5], surface enhanced Raman scattering (SERS) [6, 7] and high-harmonic generation [9], as well as in other nonlinear optics phenomena [10]. On the other hand, some plasmonic applications, such as photovoltaic devices [8] or photodetectors [11, 12], require that the involved plasmonic devices can be efficiently operated over a broadband spectrum instead of several resonant wavelengths.

A recent study has shown how transformation optics can be used to design a plasmonic nanostructure capable of efficient harvesting of light over a broadband spectrum [13]. The strategy is as follows: start with an infinite plasmonic system that naturally shows a broadband spectrum and apply a mathematical transformation that converts the infinite structure into a finite one while preserving the spectrum. This approach has been illustrated by two examples: the crescent-shaped cylinder and the kissing cylinders [13]. Some results of the analytical calculations have been presented to show the power and elegance of the conformal transformation tool. However, the demonstration has remained very general and no analytical proof has been provided. In this paper, we focus on the transformation leading to the kissing cylinders described in figure 1. The corresponding theory is derived in detail and novel physical insights are provided to explain the broadband harvesting and nanofocusing properties of this device. Note that this transformation has already been studied in the past [14, 15], but never in a plasmonics context.

IOP Institute of Physics DEUTSCHE PHYSIKALISCHE GESELLSCHAFT

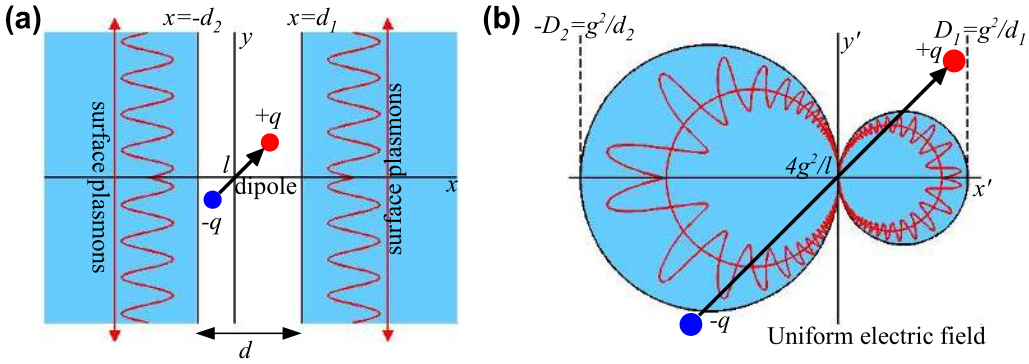


**Figure 1.** (a) Two semi-infinite metal slabs support SPPs that couple to a dipole source, transporting its energy to infinity. (b) The transformed material consists of kissing cylinders. The dipole source $\mathbf{\Delta}$ is transformed into a uniform electric field $\mathbf{E}_0$.

In this paper, we first study the coupling of a dipole with surface plasmon polaritons (SPPs) supported by two semi-infinite slabs of metal. Then, by applying a conformal transformation to this system, we deduce the behavior of SPPs in kissing cylinders and their coupling with the external field. An analytical expression of the absorption cross-section is derived. The kissing cylinders structure is an anisotropic device that may provide an efficient harvesting of light over a broadband spectrum, depending on the polarization of the incoming beam. The electric field in the transformed geometry is also expressed analytically. The SPPs propagate along the surface of the cylinders towards the touching point, where their velocity vanishes and energy accumulates. Considerable field enhancement and confinement at the nano-scale are then predicted. The nanofocusing performance results from a balance between energy accumulation and dissipation losses. The asymptotic case of a nanowire placed on top of a metal plate is shown to be of great interest for nanofocusing: a drastic field enhancement occurs over a large part of the nanowire surface and not only in the vicinity of the touching point. This analytical study relies on the near-field approximation, valid as long as the kissing cylinders are small compared to the wavelength. Consequently, numerical simulations have been performed to investigate the effect of radiative losses when the structure dimension becomes comparable to the wavelength. The cylinder pair is shown to be quite robust relative to radiation damping, its absorption cross-section remaining in the order of its physical cross-section, for dimensions up to 300 nm. Significant nanofocusing of light is also obtained for such dimensions. The case of a nanowire place on top of a metal plate is also investigated numerically. Although our theory assumes an infinite metal plate, it accurately predicts the field induced at the nanowire surface provided that the metal plate dimension is larger than half of the wavelength.

## 2. Theory

### *2.1. Conformal transformation*

Our canonical system is a line dipole that is contained in a thin slab of insulator of thickness $d = d_1 + d_2$ surrounded by two semi-infinite slabs of plasmonic material for $x < -d_2$ and $x > d_1$

(figure 1(a)). Now apply the following conformal transformation:

$$z' = \frac{g^2}{z^*}, \tag{1}$$

where $z = x + \mathrm{i}y$ is the usual complex number notation and the superscript $*$ stands for the complex conjugate. Obviously all points at infinity in $z$ translate to the origin in $z'$ and planes translate into cylinders. Hence, the resulting structure consists of two kissing cylinders (figure 1(b)). The diameters of the two cylinders are, respectively,

$$D_1 = \frac{g^2}{d_1}, \quad D_2 = \frac{g^2}{d_2}. \tag{2}$$

We also define a key parameter

$$\rho = D_1/D = \frac{d_2}{d}, \tag{3}$$

which is the ratio between one of the cylinder diameters $D_1$ and the overall size of the device, $D = D_1 + D_2$. The transformation of the source is also of particular importance. The original dipole $\mathbf{\Delta}$ is transformed into a uniform electric field [13], which we will take as due to an incident plane wave under the electrostatic approximation,

$$\mathbf{E}'_{\mathbf{0}} = \frac{1}{2\pi\epsilon_0}\frac{\mathbf{\Delta}}{g^2}. \tag{4}$$

We shall assume that the dimensions of the kissing cylinders are sufficiently small that the surface plasmon modes are well described in the near field approximation. In this case, the dielectric properties of the nanostructure are the same as those of the slab from which it is derived. Also preserved under the transformation is the electrostatic potential associated with an excitation:

$$\phi(x, y) = \phi'(x', y'). \tag{5}$$

The mathematics of the conformal transformation closely links the physics at work in each of the very different geometries. We will first solve the relatively tractable slab problem and then deduce the solution for the kissing cylinders problem.

### 2.2. *Coupling of a dipole to surface plasmons supported by metallic sheets*

The coupling of the dipole to the metallic sheets is first addressed. The near-field approximation is made; hence we assume that the Laplace equation is obeyed. The dipole $\mathbf{\Delta}$ consists of two line charges. We wish to calculate the potential $\phi$ induced on the dielectric sheets by expanding the incident field $\phi_0$ of the dipole as a Fourier series in $y$:

$$\phi_0(\mathbf{r}) = -\frac{1}{2\pi\epsilon_0}\frac{\mathbf{\Delta}\cdot\mathbf{r}}{r^2} = \frac{1}{2\pi}\int \mathrm{d}k\, \phi_0(k)\, \mathrm{e}^{\mathrm{i}ky}, \tag{6}$$

where $\phi_0(k)$ can be found by making a Fourier transform in a transverse plane at an arbitrary position $x$:

$$\phi_0(k) = \int \phi_0(x, y)\, \mathrm{e}^{-\mathrm{i}ky}\, \mathrm{d}y = \begin{cases} a_+(k)\, \mathrm{e}^{-|k|x}, & \text{if } x > 0, \\ a_-(k)\, \mathrm{e}^{|k|x}, & \text{if } x < 0, \end{cases} \tag{7}$$

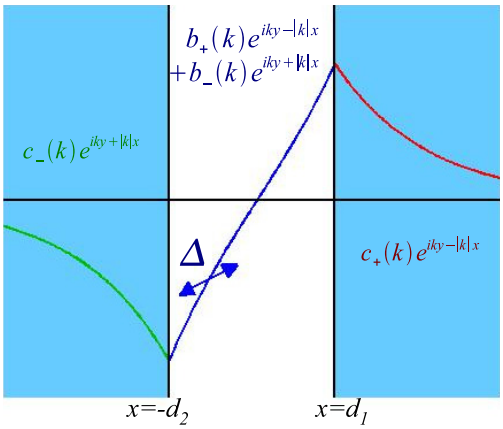


**Figure 2.** Sketch of the electrostatic potential induced by the metallic slabs when illuminated by the dipole $\boldsymbol{\Delta}$ at $x = 0$, for $\epsilon < -1$.

$$\text{with } a_\pm(k) = \frac{\mp\Delta_x + \mathrm{i}\,\mathrm{sgn}(k)\Delta_y}{2\epsilon_0}. \tag{8}$$

Next we calculate the field $\phi(k)$ induced by the metal plates when illuminated by the dipole $\boldsymbol{\Delta}$. As illustrated by figure 2, this field can be expressed as follows:

$$\phi(k) = \begin{cases} b_+(k)\,\mathrm{e}^{-|k|x} + b_-(k)\,\mathrm{e}^{|k|x}, & x > -d_2 \quad \text{and} \quad x < d_1, \\ c_+(k)\,\mathrm{e}^{-|k|x}, & x > d_1, \\ c_-(k)\,\mathrm{e}^{|k|x}, & x < -d_2. \end{cases} \tag{9}$$

The four unknowns $b_+(k)$, $b_-(k)$, $c_+(k)$ and $c_-(k)$ are then determined by the boundary conditions at the dielectric slab interfaces. Two are derived from the parallel component of the electric field being conserved at a boundary,

$$a_-(k)\,\mathrm{e}^{-|k|d_2} + b_-(k)\,\mathrm{e}^{-|k|d_2} + b_+(k)\,\mathrm{e}^{|k|d_2} = c_-(k)\,\mathrm{e}^{-|k|d_2},$$

$$a_+(k)\,\mathrm{e}^{-|k|d_1} + b_-(k)\,\mathrm{e}^{|k|d_1} + b_+(k)\,\mathrm{e}^{-|k|d_1} = c_+(k)\,\mathrm{e}^{-|k|d_1},$$

and two from conservation of the normal component of the displacement field,

$$a_-(k)\,\mathrm{e}^{-|k|d_2} + b_-(k)\,\mathrm{e}^{-|k|d_2} - b_+(k)\,\mathrm{e}^{|k|d_2} = \epsilon c_-(k)\,\mathrm{e}^{-|k|d_2},$$

$$a_+(k)\,\mathrm{e}^{-|k|d_1} - b_-(k)\,\mathrm{e}^{|k|d_1} + b_+(k)\,\mathrm{e}^{-|k|d_1} = \epsilon c_+(k)\,\mathrm{e}^{-|k|d_1}.$$

Solving these four equations provides the following results:

$$b_+(k) = -\frac{1}{2\epsilon_0}\mathrm{e}^{\alpha}\frac{\Delta_x\left(\mathrm{e}^{2|k|d_1} + \mathrm{e}^{\alpha}\right) + \mathrm{i}\,\mathrm{sgn}[k]\Delta_y\left(\mathrm{e}^{2|k|d_1} - \mathrm{e}^{\alpha}\right)}{\mathrm{e}^{2|k|d} - \mathrm{e}^{2\alpha}}, \tag{10}$$

$$b_-(k) = \frac{1}{2\epsilon_0}\mathrm{e}^{\alpha}\frac{\Delta_x\left(\mathrm{e}^{2|k|d_2} + \mathrm{e}^{\alpha}\right) - \mathrm{i}\,\mathrm{sgn}[k]\Delta_y\left(\mathrm{e}^{2|k|d_2} - \mathrm{e}^{\alpha}\right)}{\mathrm{e}^{2|k|d} - \mathrm{e}^{2\alpha}}, \tag{11}$$

$$c_+(k) = -\frac{1}{\epsilon_0}\frac{1}{\epsilon+1}\frac{\Delta_x\left(\mathrm{e}^{2|k|d_2}+\mathrm{e}^{\alpha}\right)-\mathrm{i}\,\mathrm{sgn}[k]\Delta_y\left(\mathrm{e}^{2|k|d_2}-\mathrm{e}^{\alpha}\right)}{\mathrm{e}^{2|k|d}-\mathrm{e}^{2\alpha}}, \tag{12}$$

$$c_-(k) = \frac{1}{\epsilon_0}\frac{\mathrm{e}^{2|k|d_2}}{\epsilon+1}\frac{\Delta_x\left(\mathrm{e}^{2|k|d_1}+\mathrm{e}^{\alpha}\right)+\mathrm{i}\,\mathrm{sgn}[k]\Delta_y\left(\mathrm{e}^{2|k|d_1}-\mathrm{e}^{\alpha}\right)}{\mathrm{e}^{2|k|d}-\mathrm{e}^{2\alpha}}, \tag{13}$$

where we have introduced

$$\mathrm{e}^{2\alpha} = \left(\frac{\epsilon-1}{\epsilon+1}\right)^2. \tag{14}$$

The dispersion of the excitations can be found from the condition that $b(k)$ diverges,

$$|k|d = \alpha = \begin{cases} \ln\left(\dfrac{\epsilon-1}{\epsilon+1}\right), & \text{if } \mathrm{Re}[\epsilon] < -1, \\ \ln\left(\dfrac{1-\epsilon}{\epsilon+1}\right), & \text{if } -1 < \mathrm{Re}[\epsilon] < 1. \end{cases} \tag{15}$$

This is the classical dispersion relation for SPPs in an insulator–metal–insulator structure under the near-field approximation.

Now that the induced potential is known in k-space, it can be deduced in real space via an inverse Fourier transform,

$$\phi(x,y) = \frac{1}{2\pi}\begin{cases} \displaystyle\int c_-(k)\,\mathrm{e}^{\mathrm{i}ky+|k|x}\,\mathrm{d}k, & x < -d_2, \\ \displaystyle\int \left[b_+(k)\,\mathrm{e}^{-|k|x}+b_-(k)\,\mathrm{e}^{|k|x}\right]\mathrm{e}^{\mathrm{i}ky}\,\mathrm{d}k, & -d_2 < x < d_1, \\ \displaystyle\int c_+(k)\,\mathrm{e}^{\mathrm{i}ky-|k|x}\,\mathrm{d}k, & x > d_1. \end{cases} \tag{16}$$

Let us tackle it with the field induced at the dipole, i.e. for $-d_2 < x < d_1$. By injecting the expressions of $b_+(k)$ (equation (10)) and $b_-(k)$ (equation (11)), we obtain

$$\phi(-d_2 < x < d_1) = \frac{1}{4\pi\epsilon_0}\mathrm{e}^{\alpha}\left[\Delta_x\int\frac{\left(\mathrm{e}^{2|k|d_2}+\mathrm{e}^{\alpha}\right)\mathrm{e}^{|k|x}-\left(\mathrm{e}^{2|k|d_1}+\mathrm{e}^{\alpha}\right)\mathrm{e}^{-|k|x}}{\mathrm{e}^{2|k|d}-\mathrm{e}^{2\alpha}}\mathrm{e}^{\mathrm{i}ky}\,\mathrm{d}k, \tag{17}$$

$$-\mathrm{i}\Delta_y\int\mathrm{sgn}[k]\frac{\left[\left(\mathrm{e}^{2|k|d_2}-\mathrm{e}^{\alpha}\right)\mathrm{e}^{|k|x}+\left(\mathrm{e}^{2|k|d_1}-\mathrm{e}^{\alpha}\right)\mathrm{e}^{-|k|x}\right]}{\mathrm{e}^{2|k|d}-\mathrm{e}^{2\alpha}}\mathrm{e}^{\mathrm{i}ky}\,\mathrm{d}k\Bigg]. \tag{18}$$

To perform this integration, we write

$$|k| = \lim_{\delta\to 0}\left(k^2+\delta^2\right)^{1/2}.$$

The analytic structure of equation (17) is shown in figure 3. There are two branch cuts running from $-\mathrm{i}\delta$ and $+\mathrm{i}\delta$, ensuring the analytical continuity of the integrand. The choice of these branch cuts is in agreement with the literature dealing with the calculation of Green functions in stratified media (see e.g. [16]). However, contrary to the general case, the branch cuts here only lie along the imaginary axis because of the electrostatic approximation. We shall make the approximation that the integral is dominated by either of the poles close to the real axis that correspond to surface plasmon modes carrying away energy to infinity. The cuts correspond to

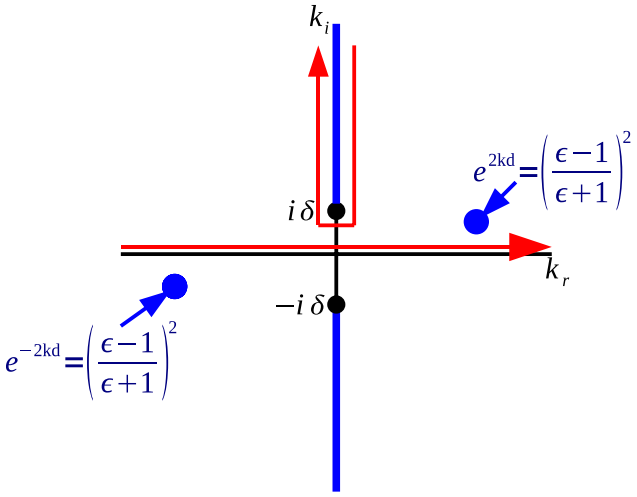


**Figure 3.** Analytic structure of the integrand of equation (17). There are two cuts running from $-i\delta$ and $+i\delta$ (blue line). There are also two poles if $\epsilon < 0$ (blue disks). If $\epsilon > 0$, these poles vanish in the cuts and give no contribution. Note that if $\epsilon < -1$, the poles are correctly placed but they swap to opposite sides of the real axis if $\epsilon > -1$.

localized virtual excitations, which, if $\epsilon$ is real, dissipate no energy. Therefore, in the limit of real $\epsilon$, our expression for dissipation will be exact, but otherwise only approximate. From now on, we will only consider the frequency band below the surface plasmon frequency, $\omega < \omega_{sp}$, for which $\epsilon < -1$. Actually, beyond $\omega_{sp}$, the imaginary part $\epsilon_I$ of the metal permittivity becomes comparable to its real part $\epsilon_R$ and the contribution from the cuts shown in figure 3 is no longer negligible. The calculation of the integral in equation (17) leads to

$$\phi(-d_2 < x < d_1) = \frac{i\Delta_x}{4d\epsilon_0}\left[\left(e^{(2\rho-1)\alpha}+1\right)e^{\alpha x/d} - \left(e^{(1-2\rho)\alpha}+1\right)e^{-\alpha x/d}\right]e^{i\alpha|y|/d} + \frac{\mathrm{sgn}[y]\Delta_y}{4d\epsilon_0}\left[\left(e^{(2\rho-1)\alpha}-1\right)e^{\alpha x/d} + \left(e^{(1-2\rho)\alpha}-1\right)e^{-\alpha x/d}\right]e^{i\alpha|y|/d}, \quad (19)$$

where we used the fact that $\rho = d_2/d$. The same technique of integration can be used to compute the field $\phi$ for $x > d_1$ and $x < -d_2$. It yields

$$\phi(x > d_1) = \frac{1}{2d\epsilon_0(\epsilon+1)}\left[-i\Delta_x\left(1+e^{(1-2\rho)\alpha}\right) + \mathrm{sgn}[y]\Delta_y\left(e^{(1-2\rho)\alpha}-1\right)\right]e^{-\alpha x/d}\,e^{i\alpha|y|/d}, \quad (20)$$

$$\phi(x < -d_2) = \frac{1}{2d\epsilon_0(\epsilon+1)}\left[i\Delta_x\left(1+e^{(2\rho-1)\alpha}\right) + \mathrm{sgn}[y]\Delta_y\left(-1+e^{(2\rho-1)\alpha}\right)\right]e^{\alpha x/d}\,e^{i\alpha|y|/d}. \quad (21)$$

### *2.3. Electric field induced at the dipole and dipolar moment of the kissing cylinders*

From the expression of the induced potential $\phi$ for $-d_2 < x < d_1$ (equation (19)), we can deduce the electric field at the dipole

$$E_x(z=0) = -\frac{\partial\phi}{\partial x}(z=0) = -\frac{i\alpha}{4d^2\epsilon_0}\Delta_x\left[e^{(2\rho-1)\alpha}+e^{(1-2\rho)\alpha}+2\right], \quad (22)$$

$$E_y(z=0) = -\frac{\partial \phi}{\partial y}(z=0) = \frac{\mathrm{i}\alpha}{4d^2\epsilon_0}\Delta_y\left[-\mathrm{e}^{(2\rho-1)\alpha} - \mathrm{e}^{(1-2\rho)\alpha} + 2\right]. \tag{23}$$

This electric field induced at the dipole is of particular interest, since it is directly related to the net dipole moment $\mathbf{p}$ of the kissing cylinders in the transformed geometry. Indeed, similarly to the relation linking the emitting dipole $\mathbf{\Delta}$ to a uniform electric field $\mathbf{E_0'}(z'=0)$ in the kissing cylinders geometry (equation (4)), the dipole moment $\mathbf{p}$ can be deduced from $\mathbf{E}(z=0)$,

$$\mathbf{p} = 2\pi\epsilon_0 g^2 \mathbf{E}(z=0). \tag{24}$$

Injecting the expression of $\mathbf{E}(z=0)$ (equations (22) and (23)) into the last equation, replacing $\mathbf{\Delta}$ by its expression (equation (4)) and using the fact that $g^2/d = \rho(1-\rho)D$ (equations (2) and (3)), the induced dipole moment can be expressed as the product of the polarizability tensor $\mathbf{\Gamma}$ with the incident electric field $\mathbf{E_0'}$ in the transformed frame:

$$\mathbf{p} = \mathbf{\Gamma}\mathbf{E_0'}, \quad \text{with} \quad \gamma_{xx} = -\mathrm{i}\pi^2\epsilon_0\alpha\rho^2(1-\rho)^2D^2\left[\mathrm{e}^{(2\rho-1)\alpha} + \mathrm{e}^{(1-2\rho)\alpha} + 2\right] \tag{25}$$

$$\text{and} \quad \gamma_{yy} = \mathrm{i}\pi^2\epsilon_0\alpha\rho^2(1-\rho)^2D^2\left[-\mathrm{e}^{(2\rho-1)\alpha} - \mathrm{e}^{(1-2\rho)\alpha} + 2\right]. \tag{26}$$

The kissing cylinders exhibit an anisotropic dipole moment, with a polarizability strongly depending on the orientation of the incoming field. Typically, for identical cylinders ($\rho = 0.5$), the dipole moment is aligned along $x'$ whatever the polarization of the incoming beam ($\gamma_{yy} = 0$).

### *2.4. Absorption cross-section*

Dipoles and fields exchange roles in the two frames, but the product is unchanged. Therefore, energy dissipation is the same in each geometry. In the slab frame, the dipole energy pumped into the SPPs in the metal slab(s) (figure 1) can be calculated from the electric field due to the excited modes evaluated at the dipole [17, 18]:

$$P = -\frac{\omega}{2}\,\mathrm{Im}\left\{\mathbf{\Delta}^* \cdot \mathbf{E}(z=0)\right\}. \tag{27}$$

This dipole power dissipated maps directly onto the power absorbed by the kissing cylinders from the uniform electric field $\mathbf{E_0'}$ that we shall take as due to an incident plane wave in the transformed frame [19]:

$$P = -\frac{\omega}{2}\,\mathrm{Im}\left\{\mathbf{E_0'}^* \cdot \mathbf{p}\right\}. \tag{28}$$

If we inject the expression of $\mathbf{p}$ (equation (25)) into the last equation, renormalize it by the incoming flux $P_{\mathrm{in}} = \epsilon_0 c_0 |\mathbf{E_0'}|^2/2$ and replace $\alpha$ by its expression as a function of the permittivity $\epsilon$ (equation (15)), then the absorption cross-section of the kissing cylinders can be deduced, for $\mathrm{Re}[\epsilon] < -1$:

$$\sigma_a^x = \pi^2 k_0 \rho^2 (1-\rho)^2 D^2 \mathrm{Re}\left\{\ln\left(\frac{\epsilon-1}{\epsilon+1}\right)\left[\left(\frac{\epsilon-1}{\epsilon+1}\right)^{1-2\rho} + \left(\frac{\epsilon-1}{\epsilon+1}\right)^{2\rho-1} + 2\right]\right\}, \tag{29}$$

$$\sigma_a^y = \pi^2 k_0 \rho^2 (1-\rho)^2 D^2 Re\left\{\ln\left(\frac{\epsilon-1}{\epsilon+1}\right)\left[\left(\frac{\epsilon-1}{\epsilon+1}\right)^{1-2\rho} + \left(\frac{\epsilon-1}{\epsilon+1}\right)^{2\rho-1} - 2\right]\right\}, \tag{30}$$

where $\sigma_a^x$ and $\sigma_a^y$ design the absorption cross-sections associated with the $x'$ and $y'$ components of the incoming field, respectively. $k_0 = \omega/c_0$ is the wave number in vacuum. Note that,

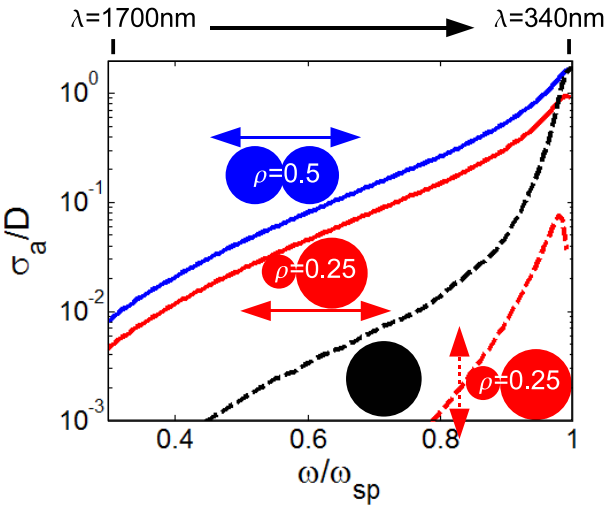


**Figure 4.** Absorption cross-section normalized by the physical cross-section $D$ as a function of frequency for kissing cylinders with $D = 20$ nm. The blue curve corresponds to the case of identical cylinders ($\rho = D_1/D = 0.5$) for an incident plane wave polarized along $x'$. The continuous and dashed red curves correspond to the case of a pair of cylinders with $\rho = D_1/D = 0.25$, with an incoming beam polarized along $x'$ and $y'$, respectively. The metal is assumed to be silver with a surface plasmon frequency $\omega_{sp} = 3.67$ eV and permittivity taken from the paper by Johnson and Christy [20]. The absorption spectrum of a single cylinder [21] with a diameter of 20 nm is also shown for comparison (dashed black line).

rigorously, this expression corresponds to the extinction cross-section of the kissing cylinders. However, as radiation losses are neglected under the quasi-static approximation, here this quantity is strictly equivalent to the absorption cross-section. $\sigma_a^{x,y}$ scales as the square of the physical size $D$ of the kissing cylinders, which is typical of a two-dimensional configuration. Figure 4 displays $\sigma_a^x$ and $\sigma_a^y$ as a fraction of the physical cross-section, for $D = 20$ nm and for different ratios between the cylinders diameters ($\rho = 0.25$ and 0.5). For this figure as well as in the following of the study, the metal is assumed to be silver with a surface plasma frequency $\omega_{sp} = 3.67$ eV and permittivity taken from the paper by Johnson and Christy [20].

As pointed out in previous studies [13, 22, 23], the kissing cylinders form a strongly anisotropic device. The $y$-polarization is particularly inefficient: equation (30) shows that $\sigma_a^y$ vanishes for identical cylinders ($\rho = 0.5$) and that $\sigma_a^y \ll \sigma_a^x$ for nanowires of different diameters. This fact is illustrated by figure 4, which compares $\sigma_a^y$ and $\sigma_a^x$ for $\rho = 0.25$.

In contrast, the cylinder pair is an efficient light harvesting device over a broadband spectrum, both in the near-infrared and visible regimes ($\lambda \sim 340 \rightarrow 1700$ nm), for an incident wave polarized along $x'$ (see figure 4). The broadband feature is highlighted by the comparison with the single cylinder case in figure 4. The fact that the two cylinders touch each other is decisive for the continuity of the spectrum. Otherwise, a resonant feature would arise, as shown by previous studies dealing with nanoparticle dimers [22]–[31]. Physically, the broadband spectrum comes from the fact that the SPPs' velocity vanishes at the touching point. SPPs are thus not reflected within the nanostructure, which prevents any resonant behavior.

For an incident polarization along $x'$, the best efficiency is found for $\rho = 0.5$, i.e. for two cylinders of the same size [13]. Even for such a small particle size ($D = 20$ nm), the absorption cross-section of kissing cylinders is of the order of the physical cross-section. For a constant ratio $\rho$, $\sigma_a/D$ scales linearly with $D$. Thus, cross-sections higher than the physical size could be obtained for larger diameter kissing cylinders but in this case our near-field analytic theory may not be valid [13]. The absorption spectrum of larger cylinders will be discussed further in section 3.2.

### 2.5. *Electric field in the transformed geometry*

A pair of kissing cylinders is a nanostructure capable of efficient harvesting of light over a broadband spectrum. As we will see now, this is also a strong far-field to near-field converter of energy, providing considerable confinement and amplification of the electric field in the vicinity of the touching point.

Under the conformal transformation, the potential is preserved (equation (5)). The electric field $\mathbf{E}'(x', y')$ in the kissing cylinders can then be easily deduced from the potential,

$$E'_{u'} = -\frac{\partial \phi}{\partial x}\frac{\partial x}{\partial u'} - \frac{\partial \phi}{\partial y}\frac{\partial y}{\partial u'}, \tag{31}$$

with $u' = x', y'$. Using the expression of the potential $\phi$ given in equations (19)–(21), the electric field $\mathbf{E}'$ can be expressed as a function of $\mathbf{E}'_0$ (equation (4)), $D$ (equation (2)) and $\rho$ (equation (3)). It yields as follows for $\epsilon < -1$.

- For $|z' - D_1/2| > D_1/2$ and $|z' + D_2/2| > D_2/2$ (outside the cylinders):

$$\begin{aligned} E'_{x'} = {} & \frac{\pi}{2}\alpha\rho^2(1-\rho)^2\frac{D^2}{(x'-\mathrm{i}|y'|)^2}\exp\left[\alpha\rho(1-\rho)\frac{D}{x'-\mathrm{i}|y'|}\right] \\ & \times\left[\mathrm{i}E'_{0x}\left(\mathrm{e}^{(2\rho-1)\alpha}+1\right)+\mathrm{sgn}[y']E'_{0y}\left(\mathrm{e}^{(2\rho-1)\alpha}-1\right)\right] \\ & +\frac{\pi}{2}\alpha\rho^2(1-\rho)^2\frac{D^2}{(x'+\mathrm{i}|y'|)^2}\exp\left[-\alpha\rho(1-\rho)\frac{D}{x'+\mathrm{i}|y'|}\right] \\ & \times\left[\mathrm{i}E'_{0x}\left(\mathrm{e}^{(1-2\rho)\alpha}+1\right)-\mathrm{sgn}[y']E'_{0y}\left(\mathrm{e}^{(1-2\rho)\alpha}-1\right)\right], \end{aligned} \tag{32}$$

$$\begin{aligned} E'_{y'} = {} & \frac{\pi}{2}\alpha\rho^2(1-\rho)^2\frac{D^2}{(x'-\mathrm{i}|y'|)^2}\exp\left[\alpha\rho(1-\rho)\frac{D}{x'-\mathrm{i}|y'|}\right] \\ & \times\left[\mathrm{sgn}[y']E'_{0x}\left(\mathrm{e}^{(2\rho-1)\alpha}+1\right)-\mathrm{i}E'_{0y}\left(\mathrm{e}^{(2\rho-1)\alpha}-1\right)\right] \\ & +\frac{\pi}{2}\alpha\rho^2(1-\rho)^2\frac{D^2}{(x'+\mathrm{i}|y'|)^2}\exp\left[-\alpha\rho(1-\rho)\frac{D}{x'+\mathrm{i}|y'|}\right] \\ & \times\left[-\mathrm{sgn}[y']E'_{0x}\left(\mathrm{e}^{(1-2\rho)\alpha}+1\right)-\mathrm{i}E'_{0y}\left(\mathrm{e}^{(1-2\rho)\alpha}-1\right)\right]. \end{aligned} \tag{33}$$

- For $|z' - D_1/2| < D_1/2$ (in the smaller cylinder):

$$\begin{aligned} E'_{x'} = {} & \pi\frac{\alpha}{\epsilon+1}\rho^2(1-\rho)^2\frac{D^2}{(x'+\mathrm{i}|y'|)^2}\exp\left[-\alpha\rho(1-\rho)\frac{D}{x'+\mathrm{i}|y'|}\right] \\ & \times\left[\mathrm{i}E'_{0x}\left(\mathrm{e}^{(1-2\rho)\alpha}+1\right)-\mathrm{sgn}[y']E'_{0y}\left(\mathrm{e}^{(1-2\rho)\alpha}-1\right)\right], \end{aligned} \tag{34}$$

$$E'_{y'} = \pi \frac{\alpha}{\epsilon+1} \rho^2 (1-\rho)^2 \frac{D^2}{(x'+\mathrm{i}|y'|)^2} \exp\left[-\alpha\rho(1-\rho)\frac{D}{x'+\mathrm{i}|y'|}\right] \times \left[-\mathrm{sgn}[y']E'_{0x}\left(\mathrm{e}^{(1-2\rho)\alpha}+1\right) - \mathrm{i}E'_{0y}\left(\mathrm{e}^{(1-2\rho)\alpha}-1\right)\right]. \quad (35)$$

- For $|z' + D_2/2| < D_2/2$ (inside the larger cylinder):

$$E'_{x'} = \pi \frac{\alpha}{\epsilon+1} \rho^2 (1-\rho)^2 \frac{D^2}{(x'-\mathrm{i}|y'|)^2} \exp\left[\alpha\rho(1-\rho)\frac{D}{x'-\mathrm{i}|y'|}\right] \times \left[\mathrm{i}E'_{0x}\left(\mathrm{e}^{(2\rho-1)\alpha}+1\right) + \mathrm{sgn}[y']E'_{0y}\left(\mathrm{e}^{(2\rho-1)\alpha}-1\right)\right], \quad (36)$$

$$E'_{y'} = \pi \frac{\alpha}{\epsilon+1} \rho^2 (1-\rho)^2 \frac{D^2}{(x'-\mathrm{i}|y'|)^2} \exp\left[\alpha\rho(1-\rho)\frac{D}{x'-\mathrm{i}|y'|}\right] \times \left[\mathrm{sgn}[y']E'_{0x}\left(\mathrm{e}^{(2\rho-1)\alpha}+1\right) - \mathrm{i}E'_{0y}\left(\mathrm{e}^{(2\rho-1)\alpha}-1\right)\right]. \quad (37)$$

Note that in the near-field approximation, which holds when the dimensions of kissing cylinders are less than the wavelength, the enhancement of electric field is independent of the size of the system. From now on, we will always consider an incident electric field polarized along $x'$, since this is the most efficient illumination. Figure 5 shows the result of our analytical calculation of the field distribution for different frequencies and ratios $\rho$. We consider the cylinder on the right as the reference (see figure 1) and hence show the field distribution with coordinates normalized by $D_1$. The metal is assumed to be silver with permittivity taken from the paper by Johnson and Christy [20].

Figures 5(a) and (b) represent the field distribution in kissing cylinders of identical and different size, respectively. These field distributions can be easily interpreted with conformal transformation, as already discussed in [13]. Here, we briefly recall the main points. In the slab frame, the surface plasmon modes transport the energy of the dipole out to infinity (see figure 1). The same modes are excited in the diametrically opposite sides of the kissing cylinders and then propagate along their surfaces. As SPPs propagate towards the touching point, their wavelength shortens and velocity decreases in proportion, similarly to what happens in sharp metallic tips or grooves [32]–[34]. Figure 5(c) represents the field distribution in the limit case of a cylinder placed on top of a metal slab ($\rho = 0$). The interpretation is slightly different compared to the kissing cylinders case. Indeed, the SPPs are excited at infinity in the metal slab and then propagate along its surface, converging from both sides towards the touching point. Of course, the infinity of the metal plate raises the question of validity of the electrostatic approximation. In practice, the metal plate will be of finite size and one can wonder how it affects the behavior of SPPs near the cylinder. This issue will be tackled with numerical simulations in section 3.4.

This qualitative account is confirmed by our analytical calculation. Considering equations (32) and (33) at the surface of the cylinder of diameter $D_1$, one can show that the phase $\phi_{\mathrm{sp}}$ of SPPs along the cylinder surface varies as

$$\phi_{\mathrm{sp}}(\theta) = \alpha(1-\rho)\tan(\theta/2), \quad (38)$$

where the angle $\theta$ is defined in the inset of figure 6. This expression confirms that the SPPs wavelength and velocity, proportional to $(\mathrm{d}\phi_{\mathrm{sp}}/\mathrm{d}\theta)^{-1}$, vanish at the structure singularity

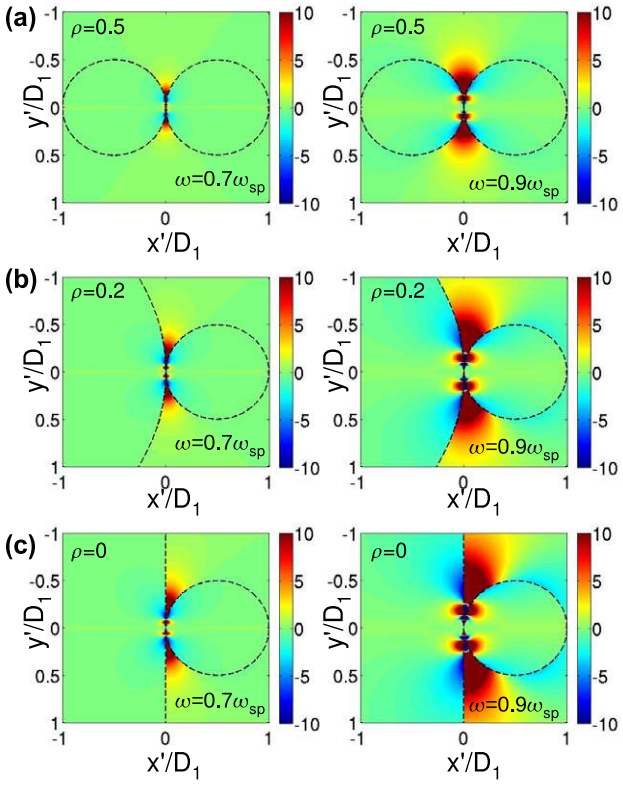


**Figure 5.** Amplitude of the real part of $E'_{x'}$ normalized by the incoming field $E'_0$ (polarized along $x'$) at different frequencies ($\omega = 0.7\omega_{sp}$ and $0.9\omega_{sp}$) and ratios of cylinders diameter ($\rho = 0.5$, 0.2 and 0). The color scale is restricted to $[-10\ 10]$, but note that the field magnitude is by far larger around the singularity of the structures.

($\theta = \pi$). The dependence in $\alpha$ is related to the dispersion relation of SPPs, which is strictly equivalent to the one derived in the slab geometry (equation (15)). Finally, the term $(1 - \rho)$ implies a decreasing of SPPs wavelength and velocity when the cylinder gets smaller than the other ($\rho < 0.5$).

In an ideal lossless metal, cancellation of the SPPs' velocity at the touching point would lead to accumulation of energy. In practice, finite loss resolves the situation, leading to a balance between energy accumulation and dissipation [13]. Figure 5 shows that the field confinement around the structure singularity strongly depends on the frequency $\omega$ and on the ratio between cylinder diameters. The physical mechanisms governing the nanofocusing performance of the kissing nanowires are discussed in the following subsection.

### *2.6. Field enhancement along the cylinders' surface*

Figure 6 shows our analytic calculation of the electric field induced at the surface of the identical cylinders by a plane wave polarized along the $x'$-axis. As pointed out previously, the wavelength of SPPs decreases as they approach the touching point, leading to an enhancement of the electric field. The growth of the field is then truncated by absorption losses at a finite angle. A considerable field enhancement of $1.15 \times 10^4$ arises here at an angle $\theta = 179.75$ deg. Also

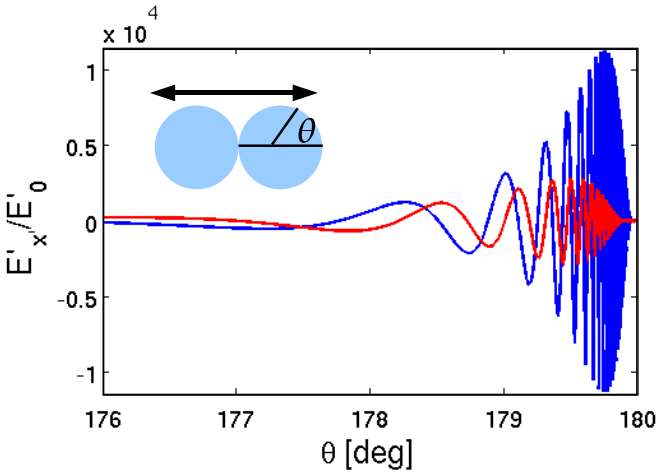


**Figure 6.** Blue curve: amplitude of the $x'$-component of the electric field at the surface of identical kissing cylinders ($\rho = 0.5$), plotted as a function of the angle, $\theta$, defined in the figure, for $\omega = 0.7\omega_{\rm sp}$ and $\epsilon = -8.3 + 0.29i$. Note that the field enhancement peaks at a finite angle. Red curve: losses are increased by a factor of two in the calculation: $\epsilon = -8.3 + 2 \times 0.29i$, resulting in less enhancement and a shift of the maximum to smaller angles. Both curves are normalized to the incoming field amplitude $E_0'$.

shown is a second calculation in which losses are increased by a factor of two, greatly reducing the enhancement and decreasing the angle at which maximum enhancement occurs.

After this brief qualitative account, a more quantitative analysis about the field enhancement can be given. The evaluation of equations (32) and (33) at the surface of the cylinder of diameter $D_1$ provides an expression of the field enhancement $|E'|/E'_{0x} = \sqrt{|E'_{x'}|^2 + |E'_{y'}|^2}/E'_{0x}$ as a function of the angle $\theta$, defined in figure 6,

$$\left|\frac{E'}{E'_{0x}}\right| = 2\pi(1-\rho)^2|\alpha|\,|\cosh[(\rho-1/2)\alpha]|\,|\cosh(\alpha)|^{1/2}\,\frac{\exp\left(-(1-\rho)\mathrm{Im}\{\alpha\}|\tan(\theta/2)|\right)}{\cos^2(\theta/2)}. \quad (39)$$

The exponential term of the last equation shows how the dissipation losses truncate the growth of the field along the cylinders' surface. From this expression of $|E'|/E'_{0x}$, the angle $\theta_{\rm max}$ at which the maximum field enhancement occurs can be easily deduced:

$$\theta_{\rm max} = \pi - \arcsin\left((1-\rho)\mathrm{Im}\{\alpha\}\right). \quad (40)$$

Using the fact that $\mathrm{Im}\{\alpha\} = \arctan(2\epsilon_{\rm I}/(|\epsilon|^2 - 1))$, $\theta_{\rm max}$ can be explicitly expressed as a function of the permittivity imaginary part $\epsilon_{\rm I}$,

$$\theta_{\rm max} \simeq \pi - \frac{2(1-\rho)\epsilon_{\rm I}}{|\epsilon|^2 - 1}, \quad \text{if } \epsilon_I \ll |\epsilon|^2 - 1. \quad (41)$$

This last equation implies a shift of the maximum field enhancement to smaller angles if the permittivity imaginary part $\epsilon_{\rm I}$ increases. In other words, dissipation losses result in a worse

confinement of the field around the structure singularity. $\theta_{\max}$ also depends on the ratio $\rho$ between cylinder diameters through the term $(1-\rho)$: when the cylinder gets smaller than the other one ($\rho \to 0$), the field tends to spread spatially along its surface. This is explained by the decrease of the SPPs' wavelength and velocity for the smallest cylinder (equation (38)): the SPPs are then absorbed before getting close to the touching point.

By injecting the expression of $\theta_{\max}$ (equation (41)) into equation (39) and replacing $\alpha$ by its expression (equation (15)), one can deduce the maximum field enhancement, $|E'_{\max}|/E'_{0x}$, that can be expected at the surface of the kissing cylinders, for $\epsilon_{\mathrm{I}} \ll |\epsilon|^2 - 1$:

$$\left|\frac{E'_{\max}}{E'_{0x}}\right| \simeq \frac{\pi}{e^2}\left|\ln\left(\frac{\epsilon-1}{\epsilon+1}\right)\left[\left(\frac{\epsilon-1}{\epsilon+1}\right)^{\rho-(1/2)}+\left(\frac{\epsilon+1}{\epsilon-1}\right)^{\rho-(1/2)}\right]\sqrt{\frac{\epsilon^2+1}{\epsilon^2-1}}\right|\frac{(|\epsilon|^2-1)^2}{\epsilon_I^2}. \tag{42}$$

The dissipation losses reduce the field enhancement as the inverse square of the permittivity imaginary part $\epsilon_{\mathrm{I}}$. This explains the ratio 4 observed between the blue and red curves in figure 6. This scaling law is of particular importance if non-local effects are not negligible and give rise to an increase of $\epsilon_{\mathrm{I}}$ [36, 37].

Figure 7(a) displays the field enhancement along the cylinders surface (equation (39)) as a function of frequency, calculated using the Johnson and Christy data [20]. At low frequencies, the field is strongly confined in the vicinity of the touching point and a spectacular field enhancement superior to $10^4$ is predicted. Then, when $\omega \to \omega_{\mathrm{sp}}$, the electric field spreads spatially and the field enhancement decreases due to higher dissipation losses.

Figure 7(b) displays the field enhancement along the cylinder surface (equation (39)) as a function of the ratio $\rho$. As explained previously, the velocity of SPPs decreases when the cylinder is smaller than the other one ($\rho < 0.5$). It implies a spatial spreading of the electric field along its surface. On the contrary, the electric field is strongly confined at the touching point in the largest cylinder frame. Interestingly, figure 7(b) shows that the magnitude of the field enhancement does not depend on the ratio $\rho$. The case of a single nanowire placed on top of a metal slab ($\rho = 0$) is thus of special interest since the field enhancement remains considerable while spreading spatially over a large part of the nanowire surface. This configuration, related to the case of rough surfaces, may find applications in SERS experiments, as already pointed out in [35].

Note that the field enhancement displayed by figure 7 may be unrealistic in practice. There are indeed two limits to our electrostatic model, as follows.

- A micro-scale limit: when the size of the device becomes comparable with the wave length, radiation losses are no longer negligible and will reduce the field enhancement induced by the nanostructure. This point will be discussed in section 3.3.
- A nano-scale limit: at small length scales, continuum electrodynamics is no longer valid and non-local effects can result in an increase of the permittivity imaginary part [36, 37]. As shown by equation (42), this increase of $\epsilon_{\mathrm{I}}$ would reduce the field enhancement compared to our theoretical prediction. Furthermore, quantum mechanical effects, such as electron tunneling or screening, have to be taken into account in the vicinity of the structure singularity and may also reduce the field enhancement relative to classical predictions [38].

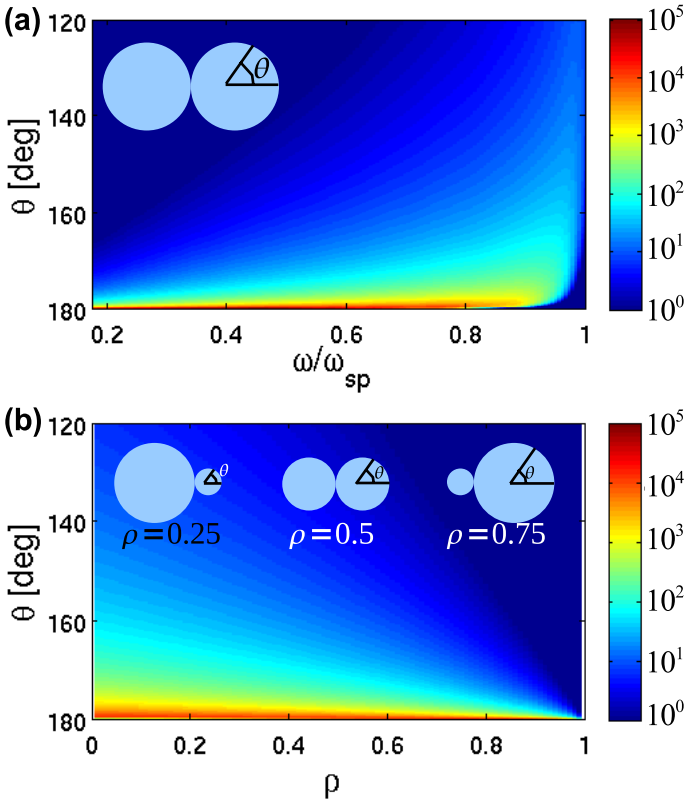


**Figure 7.** (a) Field enhancement, $|E'|/E'_0$, along the cylinder surface as a function of the angle $\theta$ and frequency, for identical cylinders. (b) Field enhancement, $|E'|/E'_0$, along the surface of the cylinder with diameter $D_1$ as a function of the angle $\theta$ and $\rho$, for $\omega = 0.75\omega_{sp}$. For both panels, the color bar is in log-scale.

## 3. Numerical simulations

We now investigate the effect of radiation losses on the harvesting and nanofocusing performances of the kissing nanowires. As already shown in [13], radiation losses make the absorption cross-section fall compared to our theoretical predictions when the structure dimension becomes comparable to the wavelength. Nevertheless, we will show, by means of numerical simulations, that the kissing cylinders structure is quite robust to radiation losses.

### *3.1. Methods*

All the numerical results presented have been obtained using COMSOL Multiphysics™, a commercial software implementing the finite element method. Two-dimensional simulations were performed within the harmonic propagation analysis mode in the frequency domain. Highly non-uniform adaptive meshes were used in order to model accurately the propagation of electromagnetic fields at the geometrical singularities of the nanostructures under study. The convergence of the numerical calculations with respect to the mesh size and the total simulation area has been checked. Mesh sides below $10^{-4}$ nm and simulation areas above $4\,\mu m^2$ were considered. As in the analytical calculations, the optical response of silver was modeled through the fit of Johnson and Christy experimental data [20].

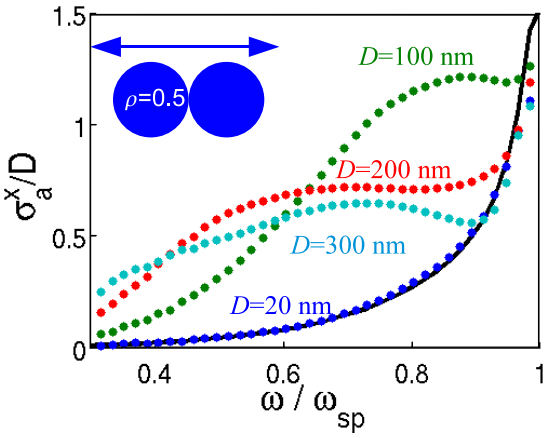


**Figure 8.** Absorption cross-section of identical kissing cylinders ($\rho = 0.5$) normalized by the physical cross-section as a function of frequency. The incident field is polarized along $x'$. The numerical absorption spectra (dots) are displayed for different structure dimensions (20, 100, 200 and 300 nm). The theoretical absorption spectrum for $D = 20$ nm is also displayed (continuous black line).

### *3.2. Kissing cylinders: absorption cross-section*

Figure 8 compares the absorption spectra obtained numerically for different sizes of kissing cylinders. For a dimension of 20 nm, the quasi-static approximation is verified and good agreement is found between numerical and analytical results. Slight disagreement occurs around the surface plasmon frequency. This is due to dissipation losses that are important in this range of frequency, whereas our theoretical model is valid in the limit $\mathrm{Im}(\epsilon) \ll -\mathrm{Re}(\epsilon)$ (see the cuts neglected in figure 3). For larger dimensions (>100 nm), radiation damping becomes important and the absorption cross-section falls compared to the theoretical prediction: electrostatic theory predicts a scaling of $\sigma_a$ as $D^2$ (equation (29)), which is clearly not the case here [13]. However, figure 8 shows that the absorption cross-section remains at least of the order of the physical cross-section, whatever the structure dimension, and can be even larger for $D = 100$ nm. As already pointed out in the literature [1], retardation effects lead to a shift of the absorption spectrum towards red compared to the electrostatic predictions. Interestingly, figure 8 indicates that the broadband behavior of the kissing cylinders is improved for large structure dimensions.

### *3.3. Kissing cylinders: field enhancement*

Figure 9 compares the field enhancement along the cylinder surface ($\rho = 0.5$) obtained numerically for different structure dimensions with our theoretical prediction. The electrostatic theory states that the field enhancement does not depend on the size of the device; hence each curve can be compared on the same basis. As observed for the absorption cross-section, there is remarkable agreement between theory and the numerical result for $D = 20$ nm. For larger structure dimension ($D > 100$ nm), radiation damping is no longer negligible and the field enhancement falls compared to our analytical prediction. However, the device still provides a significant nanofocusing of light with a maximum enhancement factor equal to $6 \times 10^3$ for $D = 300$ nm, whereas electrostatic theory predicts $1.5 \times 10^4$. The nanofocusing properties of the device are thus quite robust to radiation losses.

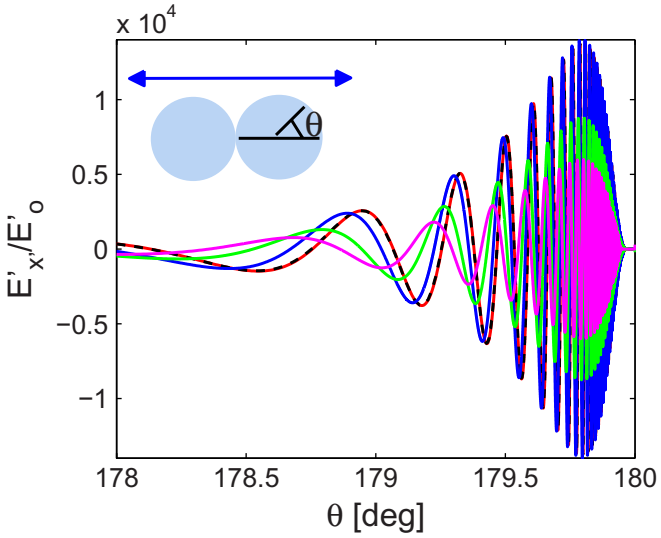


**Figure 9.** Amplitude of the $x'$-component of the electric field at the surface of one of the kissing cylinders ($\rho = 0.5$), plotted as a function of the angle, $\theta$, defined in the figure, for $\omega = 0.68\omega_{sp}$. The incident field is polarized along $x'$. The theoretical electric field (continuous red line, equation (32)) is compared to numerical results for different structure dimensions: 20 nm (dashed black curve), 100 nm (blue curve), 200 nm (green curve) and 300 nm (purple curve).

### *3.4. Nanowire on top of a metal plate*

As pointed out previously, the asymptotic case of a nanowire placed on top of a metal plate is of particular interest for light nanofocusing. However, our theory assumes a semi-infinite metal slab, whereas, experimentally, this metal plate will be of course of finite size. Consequently, numerical simulations have been performed to test the influence of the metal plate dimension. Figure 10 shows the field enhancement obtained numerically along the surface of a 10 nm cylinder for different sizes of silver plates. The numerical simulations are in good agreement with our theoretical prediction for metal plates whose characteristic size is larger than $\lambda/2$ (see the result obtained for a metal plate of $100 \times 200\,\text{nm}^2$). Below this limit, the metal plate is too small to harvest the incident energy efficiently, resulting in a lower energy density along the nanowire surface. However, even for the limit case of a $5 \times 5\,\text{nm}^2$ plate, a significant field enhancement by a factor of $5 \times 10^3$ is still obtained.

## 4. Conclusion

To conclude briefly, this study shows how a singular conformal transformation provides an elegant tool to design a plasmonic structure capable of efficient harvesting of light over the visible and near-infrared spectra. Surface plasmon modes are shown to be excited in the diametrically opposite sides of kissing cylinders and then propagate towards the touching point where the group velocity vanishes and energy accumulates. Strong field enhancement ($\sim 10^4$) and confinement are predicted within the classical approach. The nanofocusing properties of kissing nanowires have been discussed in detail. The field enhancement and confinement are the

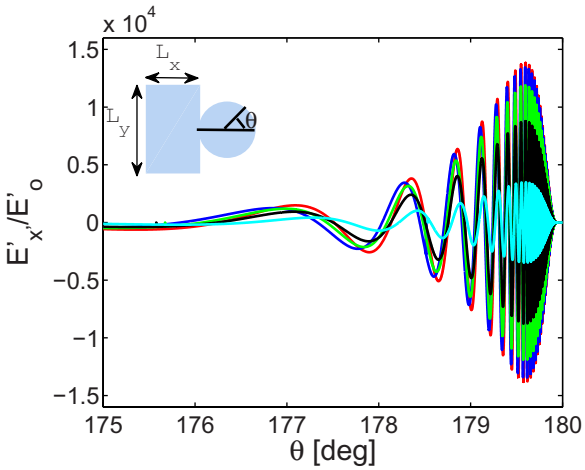


**Figure 10.** Amplitude of the $x'$-component of the electric field at the surface of the cylinder placed on top of a metal plate, plotted as a function of the angle, $\theta$, for $\omega = 0.68\omega_{sp}$. The incident field is polarized along $x'$. The theoretical electric field (continuous red line, equation (32)) is compared to numerical results for different dimensions $L_x \times L_y$ of the metal plate: $480 \times 960\,\text{nm}^2$ (blue curve), $100 \times 200\,\text{nm}^2$ (green curve), $20 \times 40\,\text{nm}^2$ (black curve) and $5 \times 5\,\text{nm}^2$ (cyan curve).

result of a balance between dissipation losses and SPPs' velocity. Numerical simulations have shown that such plasmonic structures are robust to radiation losses: the absorption cross-section is of the order of the physical cross-section over the whole visible spectrum for a structure dimension up to 300 nm. The asymptotic case of a nanowire placed on top of a metal plate has also been investigated. This configuration is of particular interest since our theory predicts a considerable field enhancement over a large part of the nanowire surface and not only in the vicinity of the touching point. Numerical simulations have shown that our theoretical prediction is valid when the metal plate characteristic dimension is, by and large, superior to half of the wavelength. The proposed plasmonic nanostructure would find great potential applications in solar cells, SERS, single molecular detection and high-harmonic generation. The experimental challenge lies in the fabrication of such a nanostructure with a nicely shaped singularity.

## Acknowledgments

This work was supported by the European Community project PHOME (contract no. 213390) and by the UK Engineering and Physical Sciences Research Council (EPSRC).

## References

[1] Maier S A 2007 *Plasmonics: Fundamentals and Applications* (New York: Springer)
[2] Schuller J A, Barnard E S, Cai W, Jun Y C, White J S and Brongersma M L 2010 Plasmonics for extreme light concentration and manipulation *Nature Mater.* **9** 193
[3] Gramotnev D K and Bozhevolnyi S I 2010 Plasmonics beyond the diffraction limit *Nature Photon.* **4** 83
[4] Nie S and Emory S R 1997 Probing single molecules and single nanoparticles by surface-enhanced Raman scattering *Science* **275** 1102

[5] Kneipp K, Wang Y, Kneipp H, Perelman L T, Itzkan I, Dasari R R and Feld M S 1997 Single molecule detection using surface-enhanced Raman scattering (SERS) *Phys. Rev. Lett.* **78** 1667
[6] Moskovits M 1985 Surface-enhanced spectroscopy *Rev. Mod. Phys.* **57** 783–826
[7] Campion A and Kambhampati P 1998 Surface-enhanced Raman scattering *Chem. Soc. Rev.* **27** 241–50
[8] Atwater H A and Polman A 2010 Plasmonics for improved photovoltaic devices *Nature Mater.* **9** 205
[9] Kim S, Jin J, Kim Y J, Park I Y, Kim Y and Kim S W 2008 High-harmonic generation by resonant plasmon field enhancement *Nature* **453** 757
[10] Bergman D J and Stockman M I 2003 Surface plasmon amplification by stimulated emission of radiation: quantum generation of coherent surface plasmons in nanosystems *Phys. Rev. Lett.* **90** 027402
[11] Tang L, Kocabas S E, Latif S, Okyay A K, Ly-Gagnon D S, Saraswat K C and Miller D A B 2008 Nanometre-scale germanium photodetector enhanced by a near-infrared dipole antenna *Nature Photon.* **2** 226
[12] Neutens P, Van Dorpe P, Vlaminck I D, Lagae L and Borghs G 2009 Electrical detection of confined gap plasmons in metal–insulator–metal waveguides *Nature Photon.* **3** 283
[13] Aubry A, Lei D Y, Fernández-Domínguez A I, Sonnefraud Y, Maier S A and Pendry J B 2010 Plasmonic light harvesting devices over the whole visible spectrum *Nano Lett.* **10** 2574–9
[14] Mc Phedran R C and Perrins W T 1981 Electrostatic and optical resonances of cylinder pairs *Appl. Phys.* **24** 311–8
[15] Mc Phedran R C and Milton G W 1987 Transport properties of touching cylinder pairs of the square array of touching cylinders *Proc. R. Soc.* A **411** 313–26
[16] Paulus M, Gay-Balmaz P and Martin O J F 2000 Accurate and efficient computation of the Green's tensor for stratified media *Phys. Rev.* E **62** 5797–807
[17] Ford G W and Weber W H 1984 Electromagnetic interactions of molecules with metal surfaces *Phys. Rep.* **113** 195–287
[18] Jun Y C, Kekatpure R D, White J S and Brongersma M L 2008 Nonresonant enhancement of spontaneous emission in metal–dielectric–metal plasmon waveguide structures *Phys. Rev.* B **78** 153111
[19] Draine B T 1988 The discrete-dipole approximation and its application to interstellar graphite grains *Astrophys. J.* **333** 848–72
[20] Johnson P B and Christy R W 1972 Optical constants of the noble metals *Phys. Rev.* B **6** 4370–9
[21] Bohren C H and Huffman D R 1983 *Absorption and Scattering of Light by Small Particles* (New York: Wiley)
[22] Kottmann J P and Martin O J F 2001 Plasmon resonant coupling in metallic nanowires *Opt. Express* **8** 655–63
[23] Kottmann J P and Martin O J F 2001 Retardation-induced plasmon resonances in coupled nanoparticles *Opt. Lett.* **26** 1096–8
[24] Hao E and Schatz G C 2004 Electromagnetic fields around silver nanoparticles and dimers *J. Chem. Phys.* **120** 357–66
[25] Enoch S, Quidant R and Badenes G 2004 Optical sensing based on plasmon coupling in nanoparticle arrays *Opt. Express* **12** 3422–7
[26] Atay T, Song J-H and Nurmikko V 2004 Strongly interacting plasmon nanoparticle pairs: from dipole–dipole interaction to conductively coupled regime *Nano Lett.* **4** 1627–31
[27] Nordlander P, Oubre C, Prodan E, Li K and Stockman M I 2004 Plasmon hybridization in nanoparticle dimers *Nano Lett.* **4** 899–903
[28] Sweatlock L A, Maier S A, Atwater H A, Penninkhof J J, Polman A and Wats T J 2005 Highly confined electromagnetic fields in arrays of strongly coupled Ag nanoparticles *Phys. Rev.* B **71** 235408
[29] Romero I, Aizpurua J, Bryant G W and García de Abajo F J 2006 Plasmons in nearly touching metallic nanoparticles *Opt. Express* **14** 9988–99
[30] Romero I, Teperik T V and García de Abajo F J 2008 Plasmon molecules in overlapping nanovoids *Phys. Rev.* B **77** 125403
[31] Britt Lassiter J, Aizpurua J, Hernandez L I, Brandl D W, Romero I, Lal S, Hafner J H, Nordlander P and Halas N J 2008 Close encounters between two nanoshells *Nano Lett.* **8** 1212–8

[32] Nerkararyan Kh V 1997 Superfocusing of a surface polariton in a wedge-like structure *Phys. Lett.* A **237** 103–5

[33] Stockman M I 2004 Nanofocusing of optical energy in tapered plasmonic waveguides *Phys. Rev. Lett.* **93** 137404

[34] Pile D F P, Ogawa T, Gramotnev D K, Okamoto T, Haraguchi M, Fukui M and Matsuo S 2005 Theoretical and experimental investigation of strongly localized plasmons on triangular metal wedges for subwavelength waveguiding *Appl. Phys. Lett.* **87** 061106

[35] García-Vidal F J and Pendry J B 1996 Collective theory of surface enhanced Raman scattering *Phys. Rev. Lett.* **77** 1163–6

[36] Kreibig U and Vollmer M 1995 *Optical Properties of Metal Clusters* (Berlin: Springer)

[37] de Abajo F J G 2008 Nonlocal effects in the plasmons of strongly interacting nanoparticles, dimers, and waveguides *J. Phys. Chem.* C **112** 17983–7

[38] Zuloaga J, Prodan E and Nordlander P 2009 Quantum description of the plasmon resonances of a nanoparticle dimer *Nano Lett.* **9** 887–91